Available online at www.sciencedirect.com

SCIENCE DIRECT®

Earth and Planetary Science Letters 213 (2003) 487–502

EPSL

www.elsevier.com/locate/epsl

Fault slip distribution of two June 2000 M_W6.5 earthquakes in South Iceland estimated from joint inversion of InSAR and GPS measurements

Rikke Pedersen [a,*], Sigurjón Jónsson [b], Thóra Árnadóttir [a], Freysteinn Sigmundsson [a], Kurt L. Feigl [c]

[a] *Nordic Volcanological Institute, Grensásvegur 50, 108 Reykjavík, Iceland*
[b] *Harvard University, Department of Earth and Planetary Sciences, 20 Oxford Street, Cambridge, MA 02138, USA*
[c] *Centre National de la Recherche Scientifique, 14 Avenue E. Belin, 31400 Toulouse, France*

Received 1 November 2002; received in revised form 22 May 2003; accepted 23 May 2003

Abstract

We present the first detailed estimates of co-seismic slip distribution on faults in the South Iceland Seismic Zone (SISZ), an area of bookshelf tectonics. We have estimated source parameters for two M_W6.5 earthquakes in the SISZ on June 17 and 21, 2000 through a joint inversion of InSAR and GPS measurements. Our preferred model indicates two simple 15 km long, near vertical faults extending from the surface to approximately 10 km depth. The geometry is in good agreement with the aftershock distribution. The dislocations experienced pure right-lateral strike-slip, reaching maxima of 2.6 m and 2.9 m for the June 17 and 21 events, respectively. We find that the distribution of slip with depth may be correlated to crustal layering, with more than 80% of the total geometric moment release occurring in the uppermost 6 km. According to the distributed slip model the middle and upper crust appears to be more apt to generate large displacements than the lower crust. The geodetic estimates of seismic moments are 4.4×10^{18} Nm (M_W6.4) and 5.0×10^{18} Nm (M_W6.5). The total moment released by the two events equals that generated by several decades of plate motion in the area, but is only a fraction of the moment accumulated in the area since the last major earthquake in 1912.

Keywords: Iceland; earthquakes; deformation; remote sensing; geodynamics; geodesy

---

1. Introduction

1.1. Tectonic setting

The complex tectonic environment in Iceland is governed by the interaction between the Icelandic mantle plume and the Mid-Atlantic Ridge, spreading at a rate of 1.9 cm/yr. The hot spot affects the spreading, creating discontinuities in

---

* Corresponding author. Tel.: +354-525-5483; Fax: +354-562-9767.
E-mail address: rikke@hi.is (R. Pedersen).

0012-821X/03/$ – see front matter © 2003 Elsevier B.V. All rights reserved.
doi:10.1016/S0012-821X(03)00302-9

the path of the ridge, which change with time. The current manifestations of the ridge on land are offset, oblique spreading segments. Two transform zones, the South Iceland Seismic Zone (SISZ) and the Tjörnes fracture zone, connect the volcanically active segments (Fig. 1A). In this paper, we study deformation in the SISZ, an E–W trending left-lateral transform zone, connecting the Eastern Volcanic Zone with the junction between the Western Volcanic Zone (WVZ) and the Reykjanes Peninsula (Fig. 1A). The SISZ extends about 70–80 km E–W and 10–15 km N–S (e.g., [2,3]). In this zone an overall left-lateral E–W motion is accommodated by right-lateral faulting on an array of parallel, N–S striking planes (Fig. 1B), a tectonic phenomenon known as bookshelf faulting (e.g., [4,5]). The presence of N–S striking, right-lateral faults was confirmed 20 years ago through field investigations carried out by Einarsson and Eiríksson [6], who mapped a number of en echelon ground ruptures striking from NNE to NE, arranged in N–S striking arrays.

1.2. Historic activity in the SISZ

Historical records going back 1100 years show that earthquakes in the SISZ tend to cluster in time. More than 30 destructive earthquakes in the area have been documented since AD 1164, either as single events, or more commonly as sequences of two or more magnitude 6–7 earthquakes over a period of days to a few years. These earthquake sequences have recurred every 45–112 years [4]. Prior to June 2000, the previous earthquake sequence took place in 1896, when five events with estimated magnitude 6–6.9 struck the area in a period of only 2 weeks (e.g., [3,4]). A single $M_S = 7$ earthquake in 1912, the first SISZ event with an instrumentally determined magnitude, occurred at the eastern border of the seismic zone [7] (Fig. 1B). The magnitudes of historical events have been evaluated through records of structural damage, in comparison with damage due to the 1912 event. The SISZ seismic sequences have a distinct pattern, where the release of energy progresses from east towards west, as observed in the 2000 sequence described below. The awareness of earthquake risk in the SISZ and consequent need for seismic monitoring continues to increase, as the population grows. As a result several projects have been initiated since the 1970s [4], e.g., a network of volumetric strain meters was installed in 1979 [8], a digital seismic network supplemented an earlier analog network in 1990 [3], and geodetic networks as described in Section 1.4.

1.3. The June 2000 events

On June 17, 2000 a $M_W6.5$ earthquake occurred in the SISZ at 15:40:51 GMT [9]. The hypocenter was located at 63.97°N, 20.37°W at 6.3 km depth [10]. Preliminary aftershock locations indicate that the earthquake occurred on a 16 km long fault, striking N09°E and dipping 86° to the east, extending from the surface to a depth of 10 km [10]. The best double-couple fault plane solution from the Harvard CMT catalog [9] has a strike of N04°E, dip 87°, and rake 173°, with a seismic moment (M_0) estimate of 7.1×10^{18} Nm corresponding to a moment magnitude (M_W) of 6.5 assuming $M_W = ((2/3) \times \log M_0) - 6.03$.

On June 21, 2000 at 00:51:55 GMT another $M_W6.5$ event occurred [9] only about 17 km west of the June 17 main shock, with a hypocenter at 63.98°N, 20.71°W and 5.1 km depth [10]. The preliminary aftershock distribution indicate that a vertical 18 km long fault ruptured, striking N02°W, extending from the surface to 8 km depth [10]. The Harvard CMT solution has a strike of N02°E, dip 85°, rake 173°, with a M_0 estimate of 5.4×10^{18} Nm, equivalent to $M_W6.5$ [9].

The two earthquakes caused major changes over a considerable area. Surface fractures, in left-stepping en echelon arrays, were abundant within several kilometers north and south of the epicenters [11]. Large strain changes were recorded in a network of volumetric strain meters, run by the Icelandic Meteorological Office (K. Ágústsson, personal communication). Geothermal water reservoirs, extensively exploited in the area, were strongly affected, with pressure changes locally in excess of 10 bar [12]. The patterns of the pressure changes are in excellent agreement with the focal mechanisms of the earthquakes, displaying a four-quadrant pattern after each event. Pressure increased significantly in areas of compres-

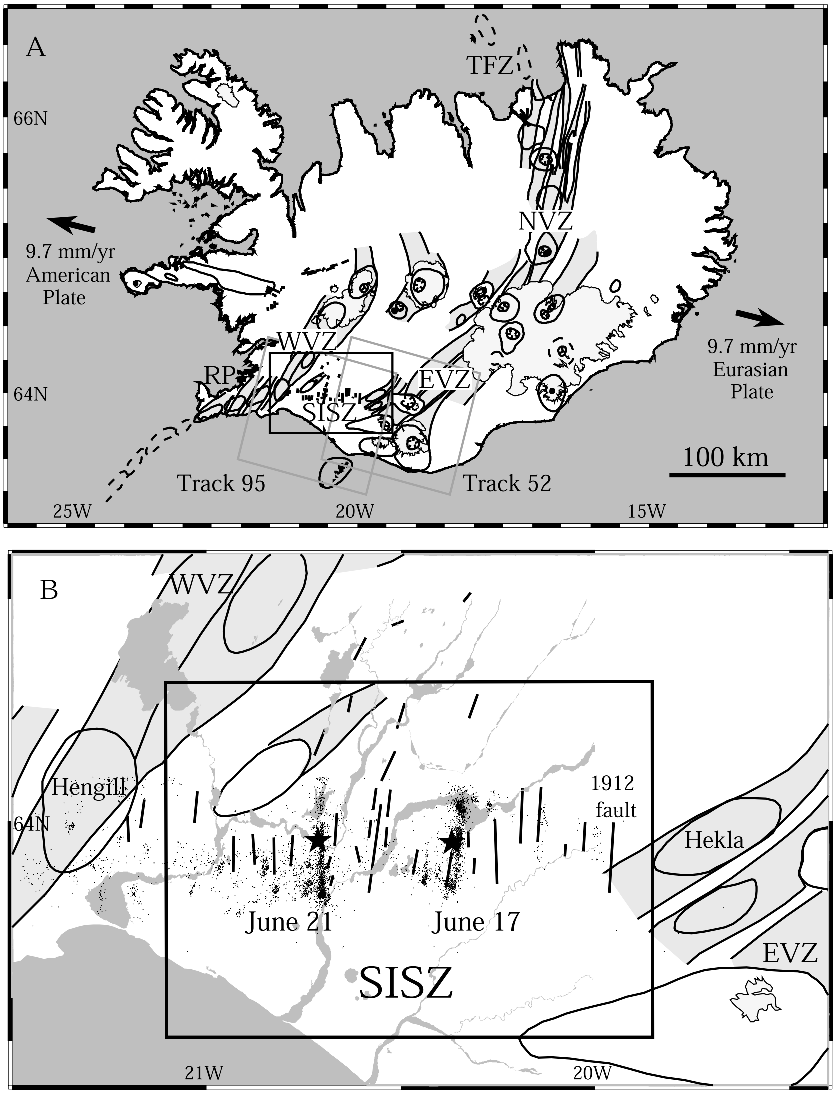

Fig. 1. (A) Map of Iceland showing the tectonic setting of the study area (modified from [1]). The locations of the Tjörnes Fracture Zone (TFZ), the Northern Volcanic Zone (NVZ), the Eastern Volcanic Zone (EVZ), the Reykjanes Peninsula (RP), the Western Volcanic Zone (WVZ) and the South Iceland Seismic Zone (SISZ) are shown. (B) A map of the SISZ (box in A). The black box delineates the extent of subsequent figures. Mapped earthquake faults are shown as black lines with the 1912 fault specified. The epicenter locations of the two June main shocks are marked with stars and aftershocks with dots.

sion (NW and SE quadrants), where some wells became artesian, and pressure decreased in dilatational areas (NE and SW quadrants) where some wells dried up. The seismicity increased markedly immediately following the June 17 event, as stress transfer triggered numerous small to intermediate earthquakes over a large area (Fig. 1B) [13]. The seismic activity propagated westward across the Reykjanes peninsula more than 80 km away, where three $M_S \approx 5$ earthquakes occurred, two apparently in response to surface wave arrivals from the June 17 main shock [14].

1.4. Previous geodetic studies of the SISZ

EDM measurements have been conducted since 1977 to study the mechanics of the SISZ. Results from 1977 to 1995 show a rather complex pattern of strain changes in the area where the two faults ruptured in 2000 [15,16]. The irregular strain pattern has been interpreted as part of a pre-seismic phase of the crustal deformation cycle [16].

Several GPS campaigns have measured deformation in the SISZ. Interseismic deformation studies based on GPS data collected between 1986 and 1992 conclude that left-lateral shear strain is accumulating across the area. Strain is concentrated in a 20–30 km wide zone where most of the 1.9 cm/year plate motion is accommodated [5]. The rate of strain accumulation is furthermore comparable to the rate of geometric moment release in earthquakes, when averaged over centuries [5].

Árnadóttir et al. [17] estimated uniform-slip fault models for the June 2000 events by inverting GPS station displacements from 1995 to 2000. Pedersen et al. [18] reported on simple slip models based on forward modeling of deformation mapped by interferometric analysis of synthetic aperture radar images (InSAR). Best-fit fault parameters for the June 17 and 21 fault models previously published [17,18] result in similar moment magnitudes and fault geometries (Table 1). Discrepancies in the fault lengths and amount of slip can be partly explained by different assumptions used in the modeling. The GPS-based model assumes that the events occurred on two distinct uniform slip planes, while the InSAR-based model presents the two fault planes, each with three superimposed slip patches of different sizes.

The purpose of this paper is to utilize the full potential of the geodetic data sets, by combining the GPS and InSAR measurements in a joint inversion procedure (e.g., [19–21]). GPS measurements are most precise for horizontal deformation, whereas the interferometric method is highly sensitive to vertical displacements. Combining these two complementary data sets helps constrain both the fault geometry and co-seismic slip distribution on the two faults better than in previous studies. From the resultant distributed slip model, we estimate the moment released during the 2000 events, which we then compare to the accumulated strain. The moment budget is important in future hazard assessments of the SISZ.

Table 1
Fault parameters for the June 2000 events estimated from different data sets

	Length (km)	Width (km)	Depth (km)	Dip (°E)	Strike (N°E)	Lon. (°)	Lat. (°)	Strike slip (m)	Dip slip (m)	Rake (°)	M_0 ($\times 10^{18}$ Nm)	M_w
June 17												
Uniform slip	10.6	7.9	0.0*	87*	1	−20.347	63.973	1.7	0	180	4.4	6.4
Distributed slip	∼15	∼10	0.0	87*	2*	−20.347	63.973	0.0–2.6	0*	180*	4.5	6.4
Árnadóttir et al. [17]	9.5	9.8	0.1	90*	3	−20.351	63.970	2.0	0.2	174	5.6	6.5
Pedersen et al. [18]	16.0	10.0*	0.0*	86*	5*	−20.342	63.979	0.3–2.4	0.0–0.2	175	5.4	6.5
NEIC [9]	–	–	–	75	−1	−20.487	63.966	–	–	173	4.3	6.4
Harvard CMT [33]	–	–	–	87	4	−20.47	63.99	–	–	−164	7.1	6.5
June 21												
Uniform slip	11.9	8.2	0.0*	90*	0	−20.705	63.987	1.8	0	180	5.3	6.4
Distributed slip	∼15	∼10	0.0	90*	0*	−20.705	63.987	0.0–2.9	0*	180*	5.0	6.5
Árnadóttir et al. [17]	12.3	8.0	0.0*	90*	0.5	−20.691	63.984	1.5	0	180	4.5	6.4
Pedersen et al. [18]	15.0	9.0*	0.0*	90*	0*	−20.703	63.982	0.5–2.2	0	180	5.1	6.4
NEIC [9]	–	–	–	79	−4	−20.758	63.980	–	–	−173	5.0	6.4
Harvard CMT [33]	–	–	–	85	2	−20.85	63.98	–	–	−167	5.4	6.5

Latitude and longitude are for the center of the fault plane at the upper edge.
*Parameter held fixed in the modeling.

2. Data

2.1. Interferograms

The ERS-2 satellite acquired all images used in this study in descending passes, with incidence angles varying from 19 to 27° across each ~100 km wide scene. Images were also acquired during ascending passes, but only post-seismic pairs could be produced. Data from two descending track frames were utilized in the modeling. Image processing was done using the PRISME/DIAPASON software [22] in the two-pass approach [23]. The digital elevation model, orbital modeling and filtering have all been described previously [24].

Interferograms can be regarded as deformation maps, where each fringe represents a change in range between ground and satellite of 2.83 cm, measured along the line of sight direction. A total of 11 image pairs covering different parts of the SISZ were analyzed, of which two co-seismic interferograms spanning 35 days each were selected for modeling (Fig. 2). These two interferograms from ERS tracks 52 and 95 are referred to as 'T52' and 'T95'.

Interferogram T52 (Fig. 2A) covers an area just east of the fault that ruptured on June 17. T52 spans the time from June 16 until July 21, and therefore records both of the large earthquakes. Only a small fraction of the June 21 deformation appears in T52, because of the distance between the June 21 epicenter and the coherent area in the interferogram. The fringes visible on the eastern side of the fault show a simple pattern of at least 15 cm of range decrease in the southern lobe and at least 12 cm of range increase in the northern lobe. The absolute maximum range change however cannot be determined due to decorrelation in the area close to the surface fault trace.

Interferogram T95 (Fig. 2B) covers a larger part of the SISZ than T52, and spans both the area affected by the June 21 event and the area of the June 17 event. This interferogram also has a time span of 35 days, from June 19 until July 24. Thus it records co-seismic deformation from the June 21 event alone, and may detect rapid post-seismic deformation in the vicinity of the June 17 fault trace.

2.2. GPS

We use station displacements from a network of 37 GPS stations, surveyed in 1995, 1999 and 2000 [17]. Data from five continuous GPS stations were included in the analysis of 1999 and 2000 data. Data acquisitions were done using dual-frequency GPS receivers, on stations occupied for approximately 24 hours, collecting data every 15 seconds. The data were analyzed using the Bernese V4.2 software package [25], and precise orbital information from the Center for Orbit Determination in Europe.

The 1995 and 2000 surveys were more extensive than the 1999 survey. Only 14 stations were measured in all three surveys. The 37 co-seismic displacement vectors (Fig. 2A) are calculated from the 1995 and 2000 station coordinates, after subtracting the interseismic motion during the 5-year period [17]. The largest horizontal GPS displacement of 0.55 m was observed near the northern end of the June 17 main rupture. The GPS stations are fairly evenly distributed in the area (Fig. 2A), and give especially valuable information west of the June 17 fault trace, where co-seismic InSAR coverage of the June 17 event is poor. The uncertainty of the GPS displacements is high as a result of the removal of the assumed interseismic model. We use an estimated uncertainty of 11–16 mm for the horizontal co-seismic displacement components and 30–40 mm for the vertical displacement components.

2.3. Data reduction and weighting

Interferogram T52 was unwrapped using Markov random field regularization and a simulated annealing optimization [26]. Interferogram T95 was unwrapped using the residue-cut unwrapping algorithm [27]. These procedures yield a large number of highly correlated data points, compared to the 37×3 components of the GPS data. We reduce the number of InSAR data by quadtree partitioning, a two-dimensional quantization algorithm (e.g., [28]) to speed up model computations. The algorithm divides the scene into four quadrants, then calculates the mean of each quadrant and subsequently evaluates the

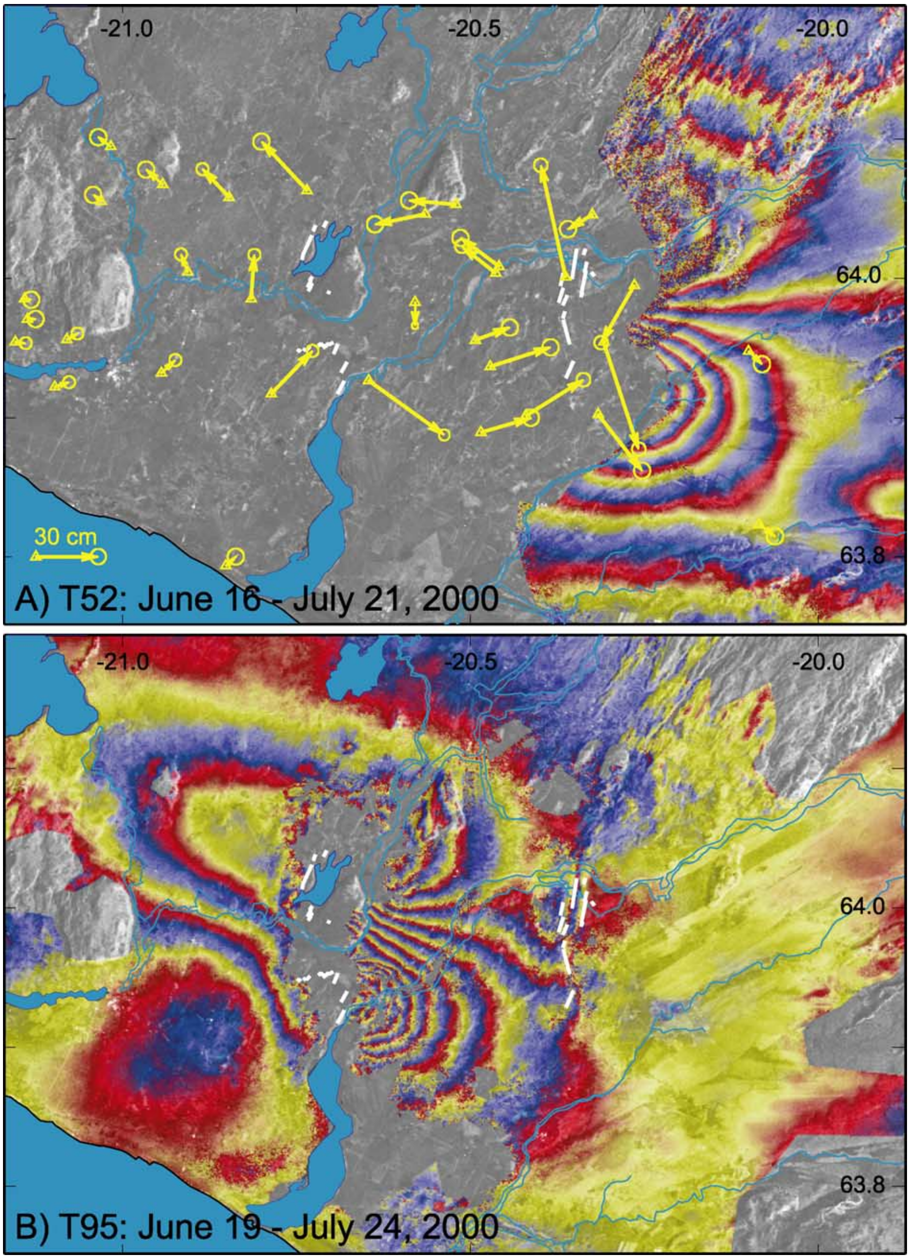

Fig. 2. Co-seismic interferograms and horizontal GPS displacements, showing ground deformation created by the June 17 and June 21 earthquakes. The images have been corrected for orbital errors. One color fringe corresponds to 2.83 cm of range change. Mapped ground ruptures are shown in white [11]. (A) Interferogram T52 spans the time from June 16 to July 21, 2000. (B) Interferogram T95 spans from June 19 to July 24, 2000.

RMS scatter against a specified threshold. The threshold was set to 10 mm for both interferograms. If the misfit exceeds the threshold, the quadrant is sub-divided into four new quadrants recursively until convergence. We estimate the standard deviation of each quadtree data point to be 13 mm through post-fit χ^2 tests. The resultant subset of the data, representing the statistically significant part of the deformation signals, is displayed in Fig. 3, with the number of data points for each data set listed in Table 2.

All observations are treated as independent with a diagonal covariance matrix. Weighting of the different data sets is determined by their estimated uncertainties, giving a relative weight of 30% and 58% for interferograms T52 and T95, and 12% in total for all three GPS components. The relatively low weight of the GPS data set reflects its spatial sparseness as well as the high uncertainty assigned to it.

3. Modeling

In the modeling, we assume that the Earth is a homogeneous and isotropic, elastic half-space containing rectangular dislocations [29]. We assume Poisson's ratio to be $\nu = 0.28$ [30], a value appropriate for the undrained conditions (where there is no fluid flow) in the fault zone immediately following the main shocks [12]. The inversion is executed in two steps. First we perform an exhaustive search for the best-fit fault parameters assuming uniform slip. Then we divide the faults into subfaults and estimate the slip on each patch.

3.1. Fault geometry estimation

Freshly formed surface ruptures were mapped in detail following the two earthquakes [11]. The right-lateral surface ruptures follow an overall N–S striking trend of en echelon left stepping fractures. However, details in the surface ruptures suggest complexities on the fault planes, especially for the June 21 event, where left-lateral slip was observed on a 500 m long central segment trending ENE [11]. The depth distribution of aftershock locations nevertheless indicates faulting on two relatively straight, near-vertical planes. We therefore begin with simple models of uniform slip on two rectangular faults.

To obtain maximum robustness in the optimal fault geometry estimation we first apply a simulated annealing algorithm followed by a derivative-based method, as recommended by Cervelli et al. [31] and described more fully by Jónsson [32].

3.1.1. Problem description

The observed ground displacements $\mathbf{d}$ can be written as a function g of the fault model parameters $\mathbf{m}$:

$$\mathbf{d} = g(\mathbf{m}) + \varepsilon \tag{1}$$

where ε are observational errors. The model vector $\mathbf{m}$ consists of 10 fault parameters for each fault: seven describe the fault plane geometry and three describe the relative displacement (slip) across the fault plane. For each event, we keep tensile opening and the upper edge fixed at 0, thereby reducing the number of free parameters to eight. This constrains the modeled earthquakes to both cut the surface and show a classic double-couple focal mechanism.

The surface displacements are a non-linear function of the fault geometry but change linearly with slip components for a fixed geometry. Accordingly, for one fault we can write Eq. 1 as:

$$\mathbf{d} = s g^{s}(\mathbf{m}') + t g^{t}(\mathbf{m}') + \varepsilon \tag{2}$$

where s and t are constant amounts of strike-slip and dip-slip respectively. The new model vector $\mathbf{m'}$ consists of the seven parameters describing the fault geometry. This system of quasi-linear equations can then be written as:

$$\begin{bmatrix} \mathbf{d}^{\mathrm{T52}} \\ \mathbf{d}^{\mathrm{T95}} \\ \mathbf{d}^{\mathrm{gps}} \end{bmatrix} = \begin{bmatrix} g^{s}(\mathbf{m}^{\mathrm{j17}}) & g^{t}(\mathbf{m}^{\mathrm{j17}}) & g^{s}(\mathbf{m}^{\mathrm{j21}}) & g^{t}(\mathbf{m}^{\mathrm{j21}}) & 1 & 0 \\ 0 & 0 & g^{s}(\mathbf{m}^{\mathrm{j21}}) & g^{t}(\mathbf{m}^{\mathrm{j21}}) & 0 & 1 \\ g^{s}(\mathbf{m}^{\mathrm{j17}}) & g^{t}(\mathbf{m}^{\mathrm{j17}}) & g^{s}(\mathbf{m}^{\mathrm{j21}}) & g^{t}(\mathbf{m}^{\mathrm{j21}}) & 0 & 0 \end{bmatrix} \begin{bmatrix} s^{\mathrm{j17}} \\ t^{\mathrm{j17}} \\ s^{\mathrm{j21}} \\ t^{\mathrm{j21}} \\ a^{\mathrm{T52}} \\ a^{\mathrm{T95}} \end{bmatrix} + \varepsilon \tag{3}$$

where vectors $\mathbf{m}^{\mathrm{j17}}$ and $\mathbf{m}^{\mathrm{j21}}$ describe the geometry of the two fault planes. Strike-slip and dip-slip values for the two faults are s^{j17}, s^{j21} and t^{j17}, t^{j21} respectively. Ambiguities (a^{T52} and a^{T95}) are introduced to correct for an arbitrary additive shift in the unwrapped data. Vectors $\mathbf{d}^{\mathrm{T52}}$ and $\mathbf{d}^{\mathrm{T95}}$ represent the displacements from the two independent interferograms and $\mathbf{d}^{\mathrm{gps}}$ is a vector

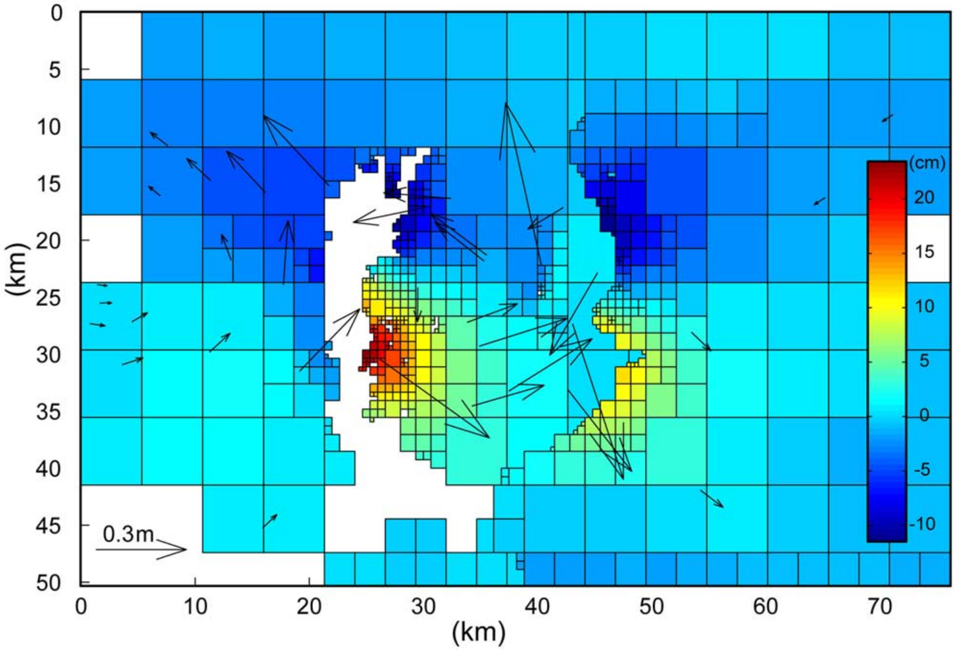

Fig. 3. Quadtree-partitioned InSAR data. The data from T52 are overlaid on T95 data. Horizontal GPS vectors are shown with black arrows.

containing the GPS displacements. The zeros in the matrix (second row, columns 1 and 2) are due to the time span of interferogram T95, which does not cover the June 17 event, and consequently has no influence on the June 17 fault parameters.

In the inversion we aim to find the model vector $\mathbf{m}$ that minimizes the L2 norm of the misfit function:

$$\Phi = \|\mathbf{W}[\mathbf{d} - g(\mathbf{m})]\|_2 \tag{4}$$

where $\mathbf{W}$ is the weight matrix from the inverse

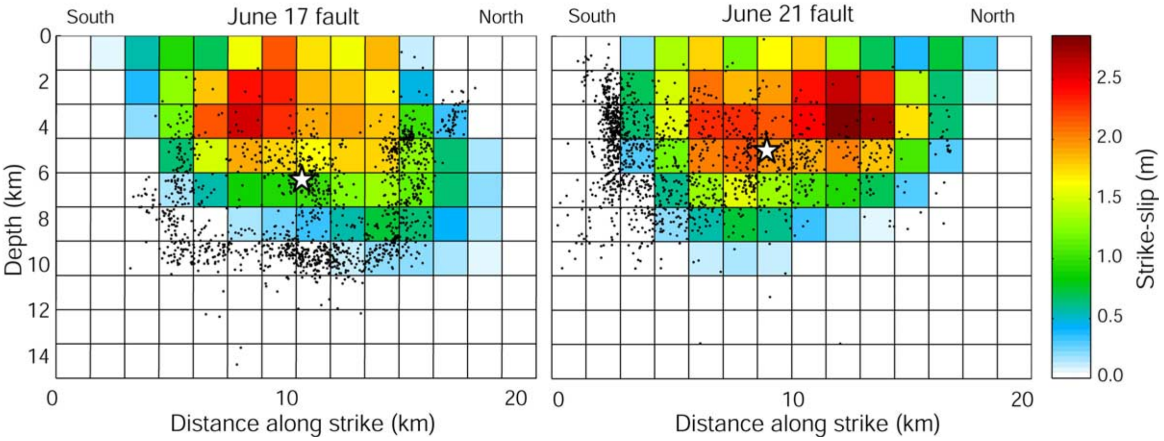

Fig. 4. Right-lateral strike-slip distribution estimated for the June 17 and June 21 earthquakes. Hypocenters are shown with white stars, and aftershocks in the immediate vicinity of the modeled fault planes as black dots. Smoothing factor $\kappa^2 = 1.4$ was used for this solution. Tests using different κ^2 values have been carried out showing that the choice of κ^2 does not significantly affect the estimated moment magnitude.

data covariance matrix $\mathbf{W}^{\mathrm{T}}\mathbf{W} = \Sigma^{-1}$ (Cholesky decomposition). We solve simultaneously for both linear and non-linear parameters by first applying simulated annealing, an effective method to find the valley containing the global minimum in the multidimensional misfit space. This Monte Carlo algorithm initially samples the model parameter space randomly [31], and progresses to search more thoroughly near recognized minima, while the randomness in the parameter search permits the algorithm to escape local minima. We then use the result as an input for a fast-converging derivative-based algorithm, which finds the bottom of the misfit valley [21]. Several separate runs are performed to ensure that the true global minimum has been located.

3.1.2. Optimal fault geometry

Initial constraints on the fault parameters in the simulated annealing searching scheme were fairly loose. However, we fixed the fault dips at 87° for the June 17 and 90° for the June 21 dislocation to match the aftershock distribution. Although dip-slip was initially allowed, it proved insignificant and was subsequently fixed to zero. Model parameters for the optimal dislocation planes estimated assuming uniform slip are found in Table 1 together with solutions from Árnadóttir et al. [17], Pedersen et al. [18], NEIC [33] and Harvard CMT [9]. We use shear modulus of 30 GPa to calculate geodetic moments and moment magnitudes from the fault slip solutions (Table 1). The simple system of two straight faults with uniform slip results in RMS misfit values of 8 mm for interferogram T52, 10 mm for T95 and 31 mm, 30 mm and 35 mm for the east, north and vertical GPS components respectively. The 729 observations in total used to estimate the 14 free parameters (six for each fault plus two additive constants) yield a χ^2_ν of 0.99. A $\chi^2_\nu = 1$ indicates an optimal fit between data and model, assuming that the prior uncertainties are realistic. The location and strike of the estimated faults resemble those of the aftershock distribution, but the length and depth of the fault planes seem to be underestimated. This discrepancy decreases when we allow the slip to taper toward the edges.

3.2. Slip distribution

Although uniform slip models can provide a fair fit to the data, we know that homogeneous slip on a sharply bounded fault plane is not physically reasonable. We obtain more realistic models by discretizing the fault planes into sub-faults and solve for slip on each patch, thereby allowing the slip to taper to zero smoothly towards the edges of the fault plane. Only strike-slip is estimated as the amount of dip-slip proved to be insignificant in the non-linear optimization.

3.2.1. Problem description

Estimating the slip distribution on a fault plane with fixed geometry is a linear problem. The optimal fault geometry obtained from the derivative-based method is used, but the fault plane is extended in both length and depth to allow for slip tapering. After discretizing the fault plane into sub-faults measuring 1.5 km × 1.5 km, we solve for the optimal slip on each patch. The problem can be written as $\mathbf{d} = \mathbf{G}\mathbf{m} + \varepsilon$, where $\mathbf{G}$ are the data kernels relating the model parameters $\mathbf{m}$ to the observed surface displacements $\mathbf{d}$. The data require weighting as before and our weighted system of equation becomes:

$$\mathbf{d}' = \mathbf{G}'\mathbf{m} \tag{5}$$

where $\mathbf{d}' = \mathbf{W}\mathbf{d}$ and $\mathbf{G}' = \mathbf{W}\mathbf{G}$. Without using an appropriate amount of smoothing, we obtain a solution with irregular slip values on adjacent patches. This arbitrary slip model may give the best fit to the data, but is unrealistic. To obtain a non-oscillatory slip distribution, we apply a smoothing constraint, which minimizes the second-order spatial derivative (Laplacian) of the fault slip (e.g., [34]). The smoothing is included by solving the system of coupled equations:

$$\begin{bmatrix} \mathbf{d}' \\ \mathbf{0} \end{bmatrix} = \begin{bmatrix} \mathbf{G}' \\ \kappa^2\mathbf{D} \end{bmatrix} \mathbf{m} \tag{6}$$

where $\mathbf{D}$ is a discrete second-order finite difference operator. The Lagrange multiplier κ^2 determines the weight of the smoothing. The full expression of Eq. 6 for this problem becomes:

$$\begin{bmatrix} \mathbf{d}'^{\mathrm{T52}} \\ \mathbf{d}'^{\mathrm{T95}} \\ \mathbf{d}'^{\mathrm{gps}} \\ \mathbf{0} \end{bmatrix} = \begin{bmatrix} d'^{\mathrm{T52}}_{1} \\ \vdots \\ d'^{\mathrm{T52}}_{n} \\ d'^{\mathrm{T95}}_{1} \\ \vdots \\ d'^{\mathrm{T95}}_{m} \\ d'^{\mathrm{gps}}_{1} \\ \vdots \\ d'^{\mathrm{gps}}_{q} \\ 0 \\ \vdots \\ 0 \\ 0 \\ \vdots \\ 0 \end{bmatrix} = \begin{bmatrix} G'^{\mathrm{T52}}_{1,1} & \cdots & G'^{\mathrm{T52}}_{1,k} & G'^{\mathrm{T52}}_{1,k+1} & \cdots & G'^{\mathrm{T52}}_{1,k+l} & 1 & 0 \\ \vdots & & \vdots & \vdots & & \vdots & \vdots & \vdots \\ G'^{\mathrm{T52}}_{n,1} & \cdots & G'^{\mathrm{T52}}_{n,k} & G'^{\mathrm{T52}}_{n,k+1} & \cdots & G'^{\mathrm{T52}}_{n,k+l} & 1 & 0 \\ 0 & \cdots & 0 & G'^{\mathrm{T95}}_{1,k+1} & \cdots & G'^{\mathrm{T95}}_{1,k+l} & 0 & 1 \\ \vdots & & \vdots & \vdots & & \vdots & \vdots & \vdots \\ 0 & \cdots & 0 & G'^{\mathrm{T95}}_{m,k+1} & \cdots & G'^{\mathrm{T95}}_{m,k+l} & 0 & 1 \\ G'^{\mathrm{gps}}_{1,1} & \cdots & G'^{\mathrm{gps}}_{1,k} & G'^{\mathrm{gps}}_{1,k+1} & \cdots & G'^{\mathrm{gps}}_{1,k+l} & 0 & 0 \\ \vdots & & \vdots & \vdots & & \vdots & \vdots & \vdots \\ G'^{\mathrm{gps}}_{q,1} & \cdots & G'^{\mathrm{gps}}_{q,k} & G'^{\mathrm{gps}}_{q,k+1} & \cdots & G'^{\mathrm{gps}}_{q,k+l} & 0 & 0 \\ \kappa^2 D_{1,1} & \cdots & \kappa^2 D_{1,k} & 0 & \cdots & 0 & 0 & 0 \\ \vdots & & \vdots & \vdots & & \vdots & \vdots & \vdots \\ \kappa^2 D_{k,1} & \cdots & \kappa^2 D_{k,k} & 0 & \cdots & 0 & 0 & 0 \\ 0 & \cdots & 0 & \kappa^2 D_{1,1} & \cdots & \kappa^2 D_{1,l} & 0 & 0 \\ \vdots & & \vdots & \vdots & & \vdots & \vdots & \vdots \\ 0 & \cdots & 0 & \kappa^2 D_{l,1} & \cdots & \kappa^2 D_{l,l} & 0 & 0 \end{bmatrix} \begin{bmatrix} s^{\mathrm{j17}}_{1} \\ \vdots \\ s^{\mathrm{j17}}_{k} \\ s^{\mathrm{j21}}_{1} \\ \vdots \\ s^{\mathrm{j21}}_{l} \\ a^{\mathrm{T52}} \\ a^{\mathrm{T95}} \end{bmatrix} \tag{7}$$

where $\mathbf{d}'^{\mathrm{T52}}$ and $\mathbf{d}'^{\mathrm{T95}}$ are the weighted data vectors of the interferograms, and $\mathbf{d}'^{\mathrm{gps}}$ the weighted GPS data vector. Subscripts n, m and q indicate the number of data points in each data set. The model vector $\mathbf{m}^{\mathrm{T}} = [(\mathbf{s}^{\mathrm{j17}})^{\mathrm{T}}, (\mathbf{s}^{\mathrm{j21}})^{\mathrm{T}}, a^{\mathrm{T52}}, a^{\mathrm{T95}}]$ consists of k slip values $\mathbf{s}^{\mathrm{j17}}$ for the June 17 fault patches, and l slip values $\mathbf{s}^{\mathrm{j21}}$ for the June 21 fault patches, as well as the ambiguities a^{T52} and a^{T95}. We solve the above system of equations with non-negative least squares [35], allowing only right-lateral strike-slip.

3.2.2. Optimal slip distribution

The preferred solution is shown in Fig. 4. The distributed slip model gives RMS misfit values of 8 mm for interferogram T52, 8 mm for T95, and 26 mm, 25 mm and 35 mm for the east, north and vertical GPS components respectively. Histograms of the residuals are plotted in Fig. 5 for model solution evaluation, with the normalized residuals for the complete data set shown in the lower right panel. The vertical GPS measurements seem to be offset by about 2 cm, though this is still within the bounds of the estimated uncertainties.

For the June 17 fault, we estimate a rupture of about 15 km in length. The slip tapers to zero at about 10 km depth, in good agreement with the aftershock locations (vertical accuracy better than 3 km; Steinunn Jakobsdóttir, personal communication, 2002). The model shows a simple slip distribution with maximum slip reaching 2.6 m. Most of the slip occurs at depths shallower than 4.5 km, just south of the hypocenter (Fig. 4). The geodetic moment is 4.5×10^{18} Nm, resulting in a M_{W} of 6.4. The June 21 modeled fault has a length of about 15 km with slip extending to about 10 km depth. Again the modeled slip distribution is consistent with the distribution of aftershock locations. The maximum slip of 2.9 m occurs slightly north of the hypocenter between 1.5 and 4.5 km depth. A second high-slip area is seen south of the hypocenter (Fig. 4). The geodetic moment is 5.0×10^{18} Nm, giving a M_{W} of 6.5. The depth to which slip extends is (in theory) dependent on the Poisson ratio assumed in the

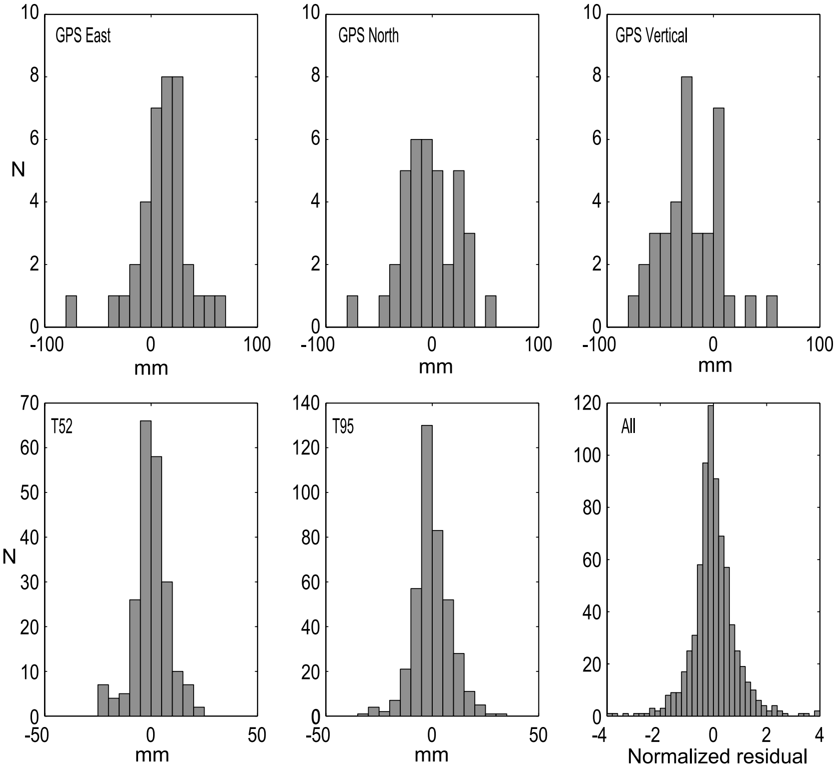

Fig. 5. Histograms of residuals for the individual data sets calculated from the distributed slip solution. The lower right panel shows the normalized residuals for the complete data set ($n = 729$).

model [36]. Slip extends slightly deeper in a material of low Poisson ratio. Due to a lower resistance to shear strain more slip at depth is then needed to reproduce the surface displacements. The actual difference between models carried out with $\nu = 0.25$ and $\nu = 0.28$ is minor in our case.

Model interferograms and GPS predictions calculated from the estimated slip distribution and associated residuals are shown in Fig. 6. The residual of interferogram T52 is close to the noise level. In the northern and southern parts of the T52 image a long wavelength residual signal is seen (Fig. 6C), most likely due to atmospheric disturbances. Interferogram T95 also shows an overall good model fit, with minor misfits in the immediate vicinity of the June 21 surface rupture, attributable to the complexities in the surface

Table 2
Number of data points, weights and RMS values of the distributed slip model

Data form	Component	Data points	Weight (%)	RMS (mm)
InSAR	T52	215	30	7
	T95	403	58	8
GPS	East	37	5	26
	North	37	5	25
	Vertical	37	2	35
Joint	All	729	100	14

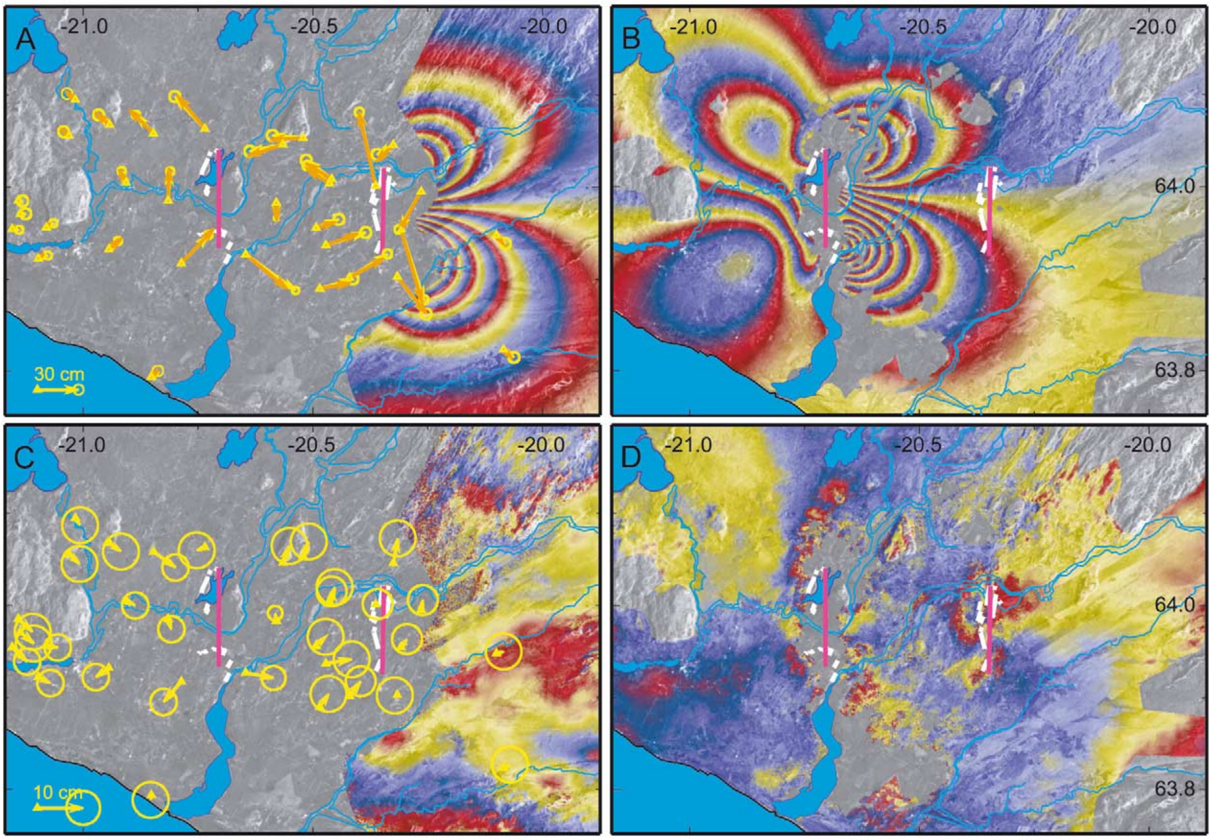

Fig. 6. Model predictions for the T52 and T95 interferograms (A,B) calculated from the distributed slip models (Fig. 4). One color fringe corresponds to 2.83 cm of range change. Observed (yellow) and predicted (orange) GPS displacements are shown in A. (C,D) Resulting residual interferograms, with residual GPS displacements in C. Note the different scales for GPS displacements in A and C. Surface ruptures are shown with white lines. The upper edges of the uniform slip model fault planes are shown with pink lines.

faulting [11] compared to our simple fault geometry. Significant residual fringes are left in the vicinity of the June 17 fault trace (Fig. 6D), showing one month of post-seismic deformation.

3.2.3. *Slip distribution resolution*

The resolution of our distributed slip solutions was examined through various checkerboard tests. Simulated data sets with added noise were inverted for distributed slip, simultaneously on both faults, as in the modeling. The results show that slip is best resolved in the uppermost 5 km. Slip details are better resolved on the June 21 fault than on the June 17 fault, due to a better spatial coverage of the June 21 event. Below 5 km, the inversion procedure smears high slip in the synthetic distribution into large areas of low slip that reach several kilometers too deep.

4. Discussion

4.1. *Aftershocks and surface rupture*

Approximately 3000 aftershock hypocenters located by the South Iceland Lowland network, between June 16 and November 22, 2000 were used to help constrain the fault dips, and subsequently to evaluate the fault lengths, widths and strikes estimated in the model. The distributions of aftershock locations agree well with the extent of fault slip on both of the modeled fault planes (Fig. 4).

The fault plane modeled for the June 21 event coincides with a plane fitted through the aftershock locations, and a dense cluster of aftershocks aligns with the southern extent of fault slip. The estimated location of the June 17 fault model is offset up to 400 m with respect to the best-fitting plane through the aftershocks. The strike of the plane estimated from the aftershock distribution is N4°E, where our optimal fault model has a strike of only N1°E. This difference is partly responsible for the offset location. The lower limits of fault slip are in good agreement with aftershock depths for both events. The simple planar geometry of the fault model appears to oversimplify complexities observed in the surface rupture. Of particular interest are the subsurface structures in the complex area south of the June 21 epicenter, where an approximately 500 m long, left-lateral, ENE trending segment of up to 2.3 m wide surface fissures was mapped [11]. In general, good correlation exists between the most extensive and continuous surface ruptures and areas of maximum slip in our distributed models (Amy Clifton, personal communication, 2002).

4.2. *Slip distribution and crustal layering*

In our models, the areas with large amounts of slip are confined to the uppermost 6 km (Fig. 4). Although resolution is better at shallower depths, checkerboard tests suggest that large slip at depth, if it occurred, would lead to an overestimate of the depth to the lower edge of the modeled fault planes. As mentioned above, the extent of the fault slip is well correlated with the distribution of aftershock depths (Fig. 4), and thus does not appear to be overestimated. If slip is focused above 6 km depth it has important implications for earthquakes in the SISZ.

Numerous studies of the thickness of the Icelandic crust have been performed over the years (e.g., [37–41]). The recent 3-D study by Allen et al. [41], using tomographic inversion of surface waves, concludes that the total thickness of the Icelandic crust ranges between 15 and 46 km, but due to the frequency window used in the study local details are not visible. A detailed study of crustal structure in SW Iceland [39] describes a three-layer structure, based on two-dimensional tomographic inversion of P-wave travel times. The crust east of the WVZ is comprised of an upper crust between 2 and 3 km thick, a middle crust 3 to 4.5 km thick and a 14–20 km thick lower crust. The upper crust consists of subaerially extruded lavas, showing increased secondary mineralization with depth. The middle crust is characterized by the appearance of heavy secondary minerals, causing an increase in the P-wave velocity. A sharp decrease in the velocity gradient defines the interface between the middle and lower crust, and prominent reflections at the bottom of the lower crust are interpreted as representing the Moho.

The areas of maximum slip in our models correspond to the complete extent of the middle and upper crust. On both the modeled faults more than 80% of the total slip occurs above 6 km depth. A layered crustal model may tend to yield a distribution with more slip at depth (e.g., [42]). The brittle part of the crust stops at the maximum hypocentral depth of the micro-seismicity. It varies smoothly across the SISZ, from 9–10 km in the west to 12–14 km in the east [3]. Stefánsson et al. [3] argue that the brittle–ductile transition zone may be shifted to greater depth during periods of large earthquakes. The June 2000 events, however, did not break into the ductile part of the crust. An important factor determining the maximum earthquake magnitude possible in the SISZ may not only be the complete thickness of the brittle regime, but also the total thickness of the upper and middle crust, as this is the section most apt to generate large displacements.

The M_S7 earthquake in 1912 occurred further east than the 2000 events, presumably in an area with thicker upper and middle crustal layers, hence a fault with a larger extent of the fault plane in the zone capable of generating large displacements. If this is a real feature of the SISZ, detailed mapping of crustal layering will be important for evaluating areas of elevated seismic hazard.

4.3. *Triggering and energy release*

Large earthquakes change the state of stress in the surrounding crust. Many studies have shown that an increase in static Coulomb stress of as little as 0.01 MPa (0.1 bar) affects aftershock locations and may trigger subsequent earthquakes if the crust is close to failure (e.g., [43]). Árnadóttir et al. [13] calculated the Coulomb stress change due to the June 17 earthquake using the distributed model obtained in this study. They found that the June 17 earthquake increased the static Coulomb stress on the hypocentral region of the (future) June 21 event by about 0.1 MPa, promoting failure on the second fault.

The historical seismicity in the SISZ has released geometric moment at the rate of 1.0–2.5×10^7 m^3/yr over the last 1000 years [5]. Since this interval includes more than 30 magnitude 6 or higher earthquakes, we assume that earthquakes release all of the strain accumulated from plate motion over the long term. Hence, we can use this same value as the rate of strain accumulation. According to our preferred models the total geometric moment released by the two main events in June 2000 is 3.1×10^8 m^3, which is less than half the 8.8–22×10^8 m^3 accumulated in the preceding 88-year interval since the last large earthquake in 1912. From 1912 to 2000 activity in the seismic zone was low. The main events in the June 2000 sequence only released stress in the seismic zone corresponding to 12–31 years of plate motion, much less than the 88 years since the occurrence of the 1912 earthquake. Further large events are to be expected in the seismic zone in the coming years or decades.

4.4. *Post-seismic deformation*

The residual signal left in Fig. 6D after removal of the distributed slip model shows that rapid post-seismic deformation took place in the vicinity of the fault activated on June 17. The post-seismic deformation field forms four quadrants, with signs opposite to those observed for the co-seismic signal. A similar pattern of post-seismic deformation was observed near the June 21 fault in an interferogram spanning June 24 to July 29, 2000 [44].

The post-seismic signal is consistent with a poro-elastic rebound model of the crust caused by pore fluid pressure changes after the earthquakes [44]. We prefer this explanation to the ‘back-slip’ model initially proposed [18]. A strong argument against ‘back-slip’ is that Coulomb failure calculations show that stress changes caused by the June 21 earthquake do not favor ‘back-slip’ on the June 17 fault. In addition, a considerable dip-slip component is required to fit the post-seismic InSAR signal with left-lateral ‘back-slip’. Co-seismic and post-seismic water level changes recorded in numerous boreholes also support poro-elastic rebound. A co-seismic water level change of more than 50 m was recorded on June 17 in the immediate vicinity of the epicenter, and a 0.5-m change occurred in a well located as far away as 75 km from the epicenter [12]. The water level recovered in most wells during the first 2 months after the earthquakes, consistent with the duration of the observed post-seismic ground movements. The poro-elastic response due to readjustment of the hydrological systems in the area has been modeled in an associated study [44].

5. Conclusions

We have estimated the fault geometry and slip distribution for two June 2000 $M_W6.5$ South Iceland earthquakes through combined inversion of InSAR and GPS data. Both earthquakes can be approximated by simple planar faults. Good correlation exists between our simplified fault plane models, aftershock hypocenters and surface ruptures. Our results show that the two right-lateral strike-slip earthquakes are very similar. The earthquakes ruptured two roughly N–S trending, near vertical 15 km long fault planes located approximately 17.5 km apart. This is consistent with the interpretation of the SISZ as an area of bookshelf tectonics, however the modeled faults are longer than previously observed in the field. The geodetic moments and slip distribution with depth are also similar for the two events. Areas of large slip are confined to the uppermost 6 km of the crust, with more than 80% of the total geometric moment release occurring above the transition from middle to lower crust. There is no geodetic evidence that brittle fracturing during the $M_W6.5$ earthquakes extends to considerably greater depth than micro-earthquake activity in the previous years.

We estimate that the total moment released in the two M_W6.5 earthquakes in June 2000 is 9.4×10^{18} Nm. This corresponds to only a fraction of the accumulated moment in the interseismic period since 1912, indicating that further large events should be expected in the seismic zone in the coming years or decades.

Acknowledgements

We would like to thank Sverrir Guðmundsson (University of Iceland) for providing the Markov random field unwrapping tools. Gunnar Guðmundsson (Icelandic Meteorological Office) kindly provided preliminary earthquake locations. We thank Amy Clifton (Nordic Volcanological Institute) and Páll Einarsson (University of Iceland) for providing data of mapped surface ruptures. Reviews by Mark Simons, Paul Lundgren, and Páll Einarsson improved the paper. The European Union supported this study through the RETINA project (EVG1-CT-00046). ERS SAR images were provided through ESA Envisat Grant A03-22 and ERS Grant A03-200. Figures 1 and 6 were produced using the GMT public domain software.***[SK]***

References

[1] P. Einarsson, K. Sæmundsson, Earthquake epicenters 1982–1985 and volcanic systems in Iceland (map), in: Th. Sigfússon (Ed.), Í Hlutarsins Eðli: Festschrift for Thorbjörn Sigurgeirsson, Menningarsjóður, Reykjavík, 1987.

[2] P. Einarsson, Earthquakes and present-day tectonism in Iceland, Tectonophysics 189 (1991) 261–279.

[3] R. Stefánsson, R. Böðvarsson, R. Slunga, P. Einarsson, S. Jakobsdóttir, H. Bungum, S. Gregersen, J. Havskov, J. Hjelme, H. Korhonen, Earthquake prediction research in the south Iceland seismic zone and the SIL project, Bull. Seismol. Soc. Am. 83 (1993) 696–716.

[4] P. Einarsson, S. Björnsson, G. Foulger, R. Stefánsson, T. Skaftadóttir, Seismicity in the South Iceland Seismic Zone, Earthquake prediction - An International Review, Maurice Ewing Series 4 (1981) 141–151.

[5] F. Sigmundsson, P. Einarsson, R. Bilham, E. Sturkell, Rift-transform kinematics in south Iceland: Deformation from Global Positioning System measurements, 1986 to 1992, J. Geophys. Res. 100 (B4) (1995) 6235–6248.

[6] P. Einarsson, J. Eiríksson, Earthquake fractures in the districts Land and Rangárvellir in the South Iceland Seismic Zone, Jökull 32 (1982) 113–119.

[7] I. Bjarnason, P. Cowie, M.H. Anders, L. Seeber, C.H. Scholz, The 1912 Iceland earthquake rupture: Growth and development of a nascent transform system, Bull. Seismol. Soc. Am. 83 (1993) 416–435.

[8] K. Ágústsson, A.T. Linde, R. Stefánsson, S. Sacks, Strain changes for the 1987 Vatnafjöll earthquake in south Iceland and possible magmatic triggering, J. Geophys. Res. 104 (B1) (1999) 1151–1161.

[9] A.M. Dziewonski, G. Ekstrom, N.N. Maternovskaya, Centroid-moment tensor solutions for April–June 2000, Phys. Earth Planet. Inter. 123 (2001) 1–14.

[10] R. Stefánsson, G.B. Guðmundsson, P. Halldórsson, The two large earthquakes in the South Iceland seismic zone on June 17 and 21, 2000, http://hraun.vedur.is/ja/skyrslur/June17and21_2000/index.html.

[11] A.E. Clifton, P. Einarsson, Styles of surface rupture accompanying the June 17 and 21, 2000 earthquakes in the South Iceland Seismic Zone, in: S.S. Jónsson (Ed.), Haustráðstefna Jarðfræðafelag Íslands 2000, Hotel Loftleiðir, 2000, p. 1.

[12] G. Björnsson, Ó.G. Flovenz, K. Saemundsson, E.M. Einarsson, Pressure changes in Icelandic geothermal reservoirs associated with two large earthquakes in June 2000, in: Proceedings of the Twenty-Sixth Workshop on Geothermal Reservoir Engineering, Stanford University, Stanford, CA, 2001.

[13] Th. Árnadóttir, S. Jónsson, R. Pedersen, G. Guðmundsson, Coulomb stress changes in the South Iceland Seismic Zone due to two large earthquakes in June 2000, Geophys. Res. Lett. 30 (2003) 1205, 10.1029/2002GL106495.

[14] C. Pagli, R. Pedersen, F. Sigmundsson, K.L. Feigl, Triggered fault slip on June 17, 2000 on the Reykjanes Peninsula, SW-Iceland captured by radar interferometry, Geophys. Res. Lett. 30 (2003) 1273, 10.1029/2002GL015310.

[15] S. Erlingsson, P. Einarsson, Distance changes in the South Iceland Seismic Zone 1977–1984, Jökull 39 (1989) 32–40.

[16] M. Lindman, Strain Precursors for the June 2000 Earthquakes, South Iceland, Masters Thesis, Luleaa University of Technology, Luleaa, 2001.

[17] T. Árnadóttir, S. Hreinsdóttir, G. Gudmundsson, P. Einarsson, M. Heinert, C. Völksen, Crustal deformation measured by GPS in the South Iceland Seismic Zone due to two large earthquakes in June 2000, Geophys. Res. Lett. 28 (2001) 4031–4034.

[18] R. Pedersen, F. Sigmundsson, K.L. Feigl, T. Árnadóttir, Co-seismic interferograms of two Ms = 6.6 earthquakes in the South Iceland Seismic Zone, June 2000, Geophys. Res. Lett. 28 (2001) 3341–3344.

[19] B. Hernandez, F. Cotton, M. Campillo, Contribution of radar interferometry to a two-step inversion of the kine-

matic process of the 1992 Landers earthquake, J. Geophys. Res. 104 (B6) (1999) 13083–13099.

[20] K.L. Feigl, F. Sarti, H. Vadon, S. Mclusky, S. Ergintav, R. Bürgmann, A. Rigo, D. Massonnet, R. Reilinger, Estimating slip distribution for the Izmit mainshock from co-seismic GPS, SPOT, and ERS-1 measurements, Bull. Seismol. Soc. Am. 92 (2002) 138–160.

[21] S. Jónsson, H. Zebker, P. Segall, F. Amelung, Fault slip distribution of the 1999 Mw7.2 Hector Mine earthquake, California, estimated from satellite radar and GPS measurements, Bull. Seismol. Soc. Am. 92 (2002) 1377–1389.

[22] C.N.E.S., DIAPASON/PRISME Software, Toulouse, 1997.

[23] D. Massonnet, K.L. Feigl, Radar interferometry and its application to changes in the Earth's surface, Rev. Geophys. 36 (1998) 441–500.

[24] K.L. Feigl, J. Gasperi, F. Sigmundsson, A. Rigo, Crustal deformation near Hengill volcano, Iceland 1993–1998: Coupling between magmatic activity and faulting inferred from elastic modeling of satellite radar interferograms, J. Geophys. Res. 105 (B11) (2000) 25655–25670.

[25] U. Hugentobler, S. Schaer, P. Friedez, Bernese GPS software, Version 4.2, Astronomical Institute, University of Berne, Berne, 2001.

[26] S. Gudmundsson, J.M. Carstensen, F. Sigmundsson, Unwrapping ground displacement signals in satellite radar interferograms with the aid of GPS data and MRF regularization, IEEE Trans. Remote Sens. Geosci. 40 (2002) 1743–1754.

[27] H.A. Zebker, Y. Lu, Phase unwrapping algorithms for radar interferometry: residue-cut, least-squares, and synthesis algorithms, J. Opt. Soc. Am. 16 (1998) 586–598.

[28] S.T. Welstead, Fractal and Wavelet Image Compression Techniques, SPIE Optical Engineering Press, Bellingham, WA, 1999, 232 pp.

[29] Y. Okada, Surface deformation due to shear and tensile faults in a half-space, Bull. Seismol. Soc. Am. 75 (1985) 1135–1154.

[30] H.F. Wang, Theory of Linear Poro-Elasticity with Applications to Geomechanics and Hydrology, Princeton University Press, Princeton, NJ, 2000, pp. 287.

[31] P. Cervelli, M.H. Murray, P. Segall, Y. Aoki, T. Kato, Estimating source parameters from deformation data, with an application to the March 1997 earthquake swarm off the Izu Peninsula, Japan, J. Geophys. Res. 106 (B6) (2001) 11217–11237.

[32] S. Jónsson, Modeling of Volcano and Earthquake Deformation from Satellite Radar Interferometric Observations, Ph.D. Thesis, Stanford University, Stanford, CA, 2002, 164 pp.

[33] U.S.G.S., National Earthquake Information Center: Previous Fast Moments, http://wwwneic.cr.usgs.gov/neis/FM/previous/0006.html.

[34] R.A. Harris, P. Segall, Detection of a locked zone at depth on the Parkfield, California, segment of the San Andreas Fault, J. Geophys. Res. 92 (B8) (1987) 7945–7962.

[35] C.L. Lawson, R. J. Hanson, Solving Least Squares Problems, Prentice-Hall, Englewood Cliffs, NJ, 1974.

[36] R. Cattin, P. Briole, H. Lyon-Caen, P. Bernard, P. Pinettes, Effects of superficial layers on co-seismic displacements for a dip-slip fault and geophysical implications, Geophys. J. Int. 137 (1999) 149–158.

[37] G. Pálmason, Crustal Structure of Iceland from Explosion Seismology, Societas Scientiarum Islandica, Reykjavík, 1971, 187 pp.

[38] Ó.G. Flóvenz, K. Gunnarsson, Seismic crustal structure in Iceland and surrounding area, Tectonophysics 189 (1991) 1–17.

[39] I.T. Bjarnason, W. Menke, Ó.G. Flóvenz, D. Caress, Tomographic image of the mid-Atlantic plate boundary in Southwestern Iceland, J. Geophys. Res. 98 (1993) 6607–6622.

[40] W. Menke, V. Levin, Cold crust in a hot spot, Geophys. Res. Lett. 21 (1994) 1967–1970.

[41] R.M. Allen, G. Nolet, W. Jason Morgan, K. Vogfjörd, M. Nettles, G. Ekström, B.H. Bergsson, P. Erlendsson, G.R. Foulger, S. Jakobsdóttir, B.R. Julian, M. Pritchard, S. Ragnarsson, R. Stefánsson, Plume driven plumbing and crustal formation in Iceland. J. Geophys. Res. 107 (B8) (2002) 2163, 10.1029/2001JB000584.

[42] M. Simons, Y. Fialko, L. Rivera, Co-seismic deformation from the 1999 M_W 7.1 Hector Mine, California, earthquake as inferred from InSAR and GPS observations, Bull. Seismol. Soc. Am. 92 (2002) 1390–1402.

[43] R. Harris, Introduction to special section: Stress triggers, stress shadows, and implications for seismic hazard, J. Geophys. Res. 103 (1998) 24347–24358.

[44] S. Jónsson, P. Segall, R. Pedersen, G. Björnsson, Post-earthquake ground movements correlated to pore-pressure transients, Nature (2003) in press.